Supporting Information

for

How Soft Metal Halide Perovskite Lattices Heal Following Energetic Particle Bombardment

Kumar Miskin, Gerard Lemson, Thomas Arbaugh, E. Ragusa, Nam Q. Le, and Paulette Clancy

Contents

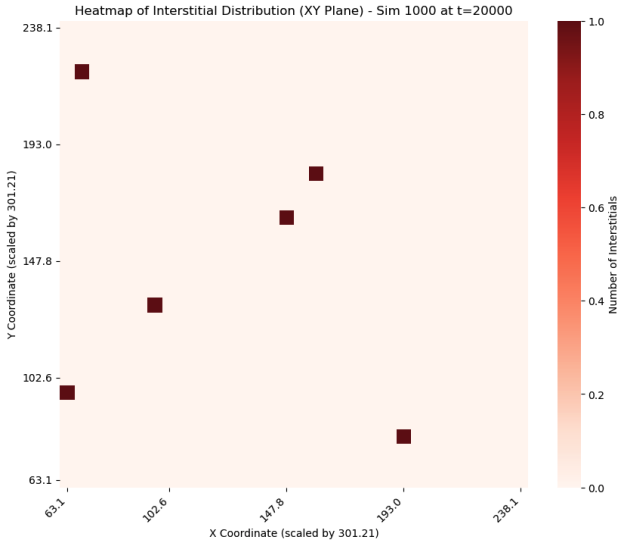

Figure 1: Spatial distribution of interstitial defects in the xy plane following an energetic particle impact. Heat map showing the spatial distribution of interstitials in the xy plane for the 1000 eV impact simulation at a time, t = 20,000 fs near the end of the simulation. The simulation cell is divided into a 32 $\times$ 32 grid of pixels. The color scale on the RHS indicates the number of interstitial atoms falling within each spatial bin. Coordinates are scaled by the full simulation box length (301.21 Å). Interstitials are sparsely distributed and are notably absent from the immediate vicinity of the impact center, indicating that atoms displaced during the collision cascade are transported away from the primary impact region rather than accumulating locally.

1 Limitations of the Classical ReaxFF Approach

There are some limitations of the semi-empirical ReaxFF framework used here that warrant explicit discussion. First, ReaxFF is a bond-order empirical potential and does not represent electronic degrees of freedom. Consequently, inelastic electronic energy loss (electronic stopping) and electron-phonon coupling, which formally require a two-temperature model (TTM) treatment (Nordlund et al., 2018), are absent from our simulations. Electronic stopping becomes the dominant energy loss channel for swift ions only at MeV-range energies. For protons incident on heavy-atom semiconductor targets, Monte Carlo transport simulations confirm that nuclear stopping, quantified as non-ionizing energy loss (NIEL), dominates over electronic stopping across the entire sub-keV energy range, with the crossover to electronic-stopping dominance occurring only at projectile energies well above 100 keV per nucleon (Fan et al., 2022; Ziegler and Biersack, 1985). This is consistent with the radiation testing guidelines of Kirmani et al. (2022), which explicitly distinguish the nuclear displacement and electronic ionization regimes and identify the former as dominant at low irradiation energies. For the 1 eV to 1 keV PKA recoil energies studied here, nuclear stopping is unambiguously dominant, and the omission of an electronic stopping correction introduces negligible error

in the predicted defect populations and structural distortions reported in this work. At higher irradiation energies ($\gtrsim$10 keV), electronic stopping corrections would become necessary, and future work extending this study to the MeV-range space radiation environment should incorporate a TTM or ZBL-corrected potential.

Stochastic electron scattering and ionization track effects, which can drive Coulombic explosion and local charge redistribution in ionic materials, are not captured by any classical potential framework including ReaxFF (Nordlund et al., 2018). Experimental studies of MHP radiation tolerance have identified electronic ionization as a distinct and sometimes competing degradation channel, particularly under high-fluence proton or electron irradiation (Durant et al., 2021). For the sub-keV nuclear stopping regime studied here, these ionization-driven effects are expected to be secondary relative to ballistic displacement processes; however, they represent a known limitation of the classical MD approach and would need to be accounted for in any future extension of this work to MeV-range swift ion irradiation, where ionization tracks become the dominant damage mechanism (Kirmani et al., 2022).

Second, the ReaxFF parameterization of Pols et al. (2021) was validated against DFT-generated structural properties, bond energetics, and point defect geometries in $CsPbI_3$ under near-equilibrium conditions, rather than being specifically created for high-energy collision cascades. While cascade-specific validation remains an open challenge for any MHP interatomic potential, two independent lines of evidence support the physical relevance of our results. First, the octahedral tilt distributions predicted by our MD simulations map quantitatively onto classical Glazer tilt systems that are experimentally observed in $CsPbI_3$ nanocrystals and thin films, suggesting that the force field correctly describes the soft-mode response of the PbI_6 network. Second, the dominance of iodine displacements and the relative resilience of the Pb sublattice are consistent with the known low formation energies of halide Frenkel pairs in MHPs (Kang and Wang, 2017) and with experimental radiation hardness data for this class of material (Delmas et al., 2023).

Finally, the energy dissipation mechanism identified here, namely the preferential accommodation of impact energy through collective rotational and tilting modes of the PbI_6 octahedral network, reflects a physical consequence of the anomalously soft low-frequency phonon branches that are characteristic of MHPs and that are well reproduced by the ReaxFF model (Pols et al., 2021). We regard this as a robust qualitative finding rather than a force-field artifact, while acknowledging that the precise quantitative values of tilt angles and recovery fractions carry uncertainties associated with the classical description. Importantly, independent support for the physical reality of this mechanism comes from a recent machine-learned interatomic potential study by Farigliano et al. (2026), who observed precessional dynamics of $PbBr_6$ octahedra in $CsPbBr_3$ using an MLIP trained on ab initio data. This is fully con-

sistent with the collective rotational and tilting modes we have identified here using ReaxFF. The agreement between two independent and methodologically distinct frameworks strengthens confidence that this dissipation mechanism reflects genuine lattice physics. Future work incorporating machine-learned interatomic potentials (MLIPs) trained on radiation-relevant configurations could provide a path toward reducing these uncertainties while retaining the computational tractability required for cascade-scale simulations.

2 Energetic Particle Impact Protocol

Radiation damage was modeled using a primary knock-on atom (PKA) approach. A hemispherical region centered at the top free surface of the slab was selected as the impact zone. Atoms within a radius of 5 Å from the impact center were assigned an initial kinetic energy corresponding to the desired PKA energy.

Eight PKA energies were investigated: 1, 10, 25, 50, 75, 100, 500, and 1000 eV. These energies span the range relevant to energetic particle interactions in low-Earth orbit. Following energy deposition, the system dynamics were allowed to evolve for 10,000 time steps (*i.e.,* 10 *ps*), during which atomic trajectories, velocities, charges, and per-atom energies were calculated and recorded at each time step. Longer simulation times were impractically resource-intensive for a system as large as this.

3 Limitations to alternate approaches to model radiation damage

An alternative approach would be to include the incident ion (*e.g.,* a proton or ^{4}He nucleus) as an explicit atom in the simulation and propagate it through the target as shown by Nguyen et al. in 2023. This has the advantage of naturally capturing the spatial distribution of energy deposition along the ion trajectory and can, in principle, reproduce Bragg-peak effects at higher energies. However, it introduces significant challenges in the present context: accurate simulation of a fast light ion interacting with a heavy-atom lattice such as $CsPbI_3$ requires an electronic stopping correction—typically implemented via a Ziegler–Biersack–Littmark (ZBL) potential shown by Nordlund et al. in 2018 or equivalent—that is not parameterized within the ReaxFF framework used here. Without such a correction, the electronic energy loss of the projectile is not accounted for, leading to an overestimate of nuclear energy deposition and an unphysical treatment of the ion trajectory. Furthermore, for the sub-keV energy range we investigate, the projected range of a proton or helium ion in $CsPbI_3$ is on the order of tens of nanometers or less, meaning that the PKA approximation and the explicit ion

approach converge to the same physical regime of primary damage. We therefore conclude that the PKA recoil cascade methodology is the appropriate and well-justified choice for this study, and that the inclusion of explicit ion trajectories is a natural extension for future work at higher (MeV-range) energies where electronic stopping becomes the dominant energy loss channel.

4 Spatial Distribution of Vacancies and Interstitials After Impact

To further elucidate the nature of primary radiation damage and subsequent defect redistribution, we analyzed the spatial distributions of vacancies and interstitials in the xy plane following a high-energy (1000 eV) impact event. Figures S1 and S4 present "heat maps" of interstitial and vacancy populations, respectively, evaluated at time, t = 20,000 fs, after the system has undergone initial ballistic damage and partial relaxation.

A pronounced asymmetry is observed between vacancy and interstitial distributions. Vacancies are created at, and highly concentrated near, the center of the impact region, forming a localized damage core. This behavior is consistent with the primary knock-on atom displacing lattice atoms from their equilibrium positions, thereby creating a dense population of vacant lattice sites in the immediate vicinity of energy deposition.

In contrast, interstitials are comparatively sparse and are distributed over a much larger lateral area, with a notable depletion near the impact center itself. This spatial separation reflects the ballistic nature of the collision cascade: atoms displaced by the incident energy acquire sufficient kinetic energy to migrate away from the impact site before becoming trapped at interstitial positions elsewhere in the lattice. As a result, the impact region is vacancy-rich and interstitial-poor, while displaced atoms are redistributed throughout the surrounding bulk.

The dominance of vacancies relative to interstitials near the impact center is an expected consequence of momentum transfer and mass transport during irradiation. This separation of defect species has important implications for defect recombination and self-healing processes. Vacancy-rich regions provide a strong thermodynamic driving force for subsequent lattice relaxation, while the spatially dispersed interstitials may later migrate back toward vacant sites or participate in more complex defect reactions during longer-time annealing processes. But this is beyond an accessible time scale in the present simulations.

These spatial maps provide a clear, intuitive picture of how energetic particle impacts generate nonuniform defect landscapes in metal halide perovskites, complementing the octahedral distortion and angular disorder analyses presented in the main text.

5 Anti-site formation

To quantify the extent of anti-site defect formation following energetic perturbations, we analyzed atomic displacements relative to ideal crystallographic sublattice positions. An atom was classified as an anti-site if it occupied an incorrect sublattice position within 1 Å of the corresponding ideal lattice site. This stringent geometric criterion ensures that only well-defined anti-site configurations are counted, excluding transient or highly displaced atoms that do not represent stable site exchange.

Figure 2 summarizes anti-site formation for Cs, Pb, and I atoms as a function of incident energy. While the total number of displaced atoms increases substantially with energy for all species, the fraction that relax into anti-site configurations remains extremely small.

For Cs, anti-sites are only observed at the highest simulated energy (1000 eV), corresponding to 4–5% of displaced Cs atoms. For I, anti-sites appear at 500 and 1000 eV but remain limited to 1–2% of displaced atoms. Notably, Pb anti-site formation is absent within a <1 Å definition across all energies considered.

These results demonstrate that PKA events do not efficiently generate stable anti-site defects in this system. Instead, most displaced atoms either remain as vacancies or interstitials, form more complex defect clusters, or relax back toward their original sublattice positions without completing a site exchange. The energetic and structural constraints of the perovskite lattice therefore strongly suppress anti-site stabilization, even under high-energy perturbations.

6 Steinhardt Bond Orientational Order Parameters

Local orientational order was quantified using the Steinhardt bond order parameters q_ℓ, defined as:

$$q_\ell(i) = \left(\frac{4\pi}{2\ell+1} \sum_{m=-\ell}^{\ell} |q_{\ell m}(i)|^2 \right)^{1/2}, \tag{1}$$

where

$$q_{\ell m}(i) = \frac{1}{N(i)} \sum_{j=1}^{N(i)} Y_{\ell m}(\hat{r}_{ij}). \tag{2}$$

Here, $Y_{\ell m}$ are spherical harmonics, $N(i)$ is the number of nearest neighbors of atom i, and $\hat{r}_{ij}$ is the unit vector connecting atom i to neighbor j. We computed q_4 and q_6 for Pb atoms using their six nearest iodine neighbors to probe distortions of the PbI_6 octahedral framework.

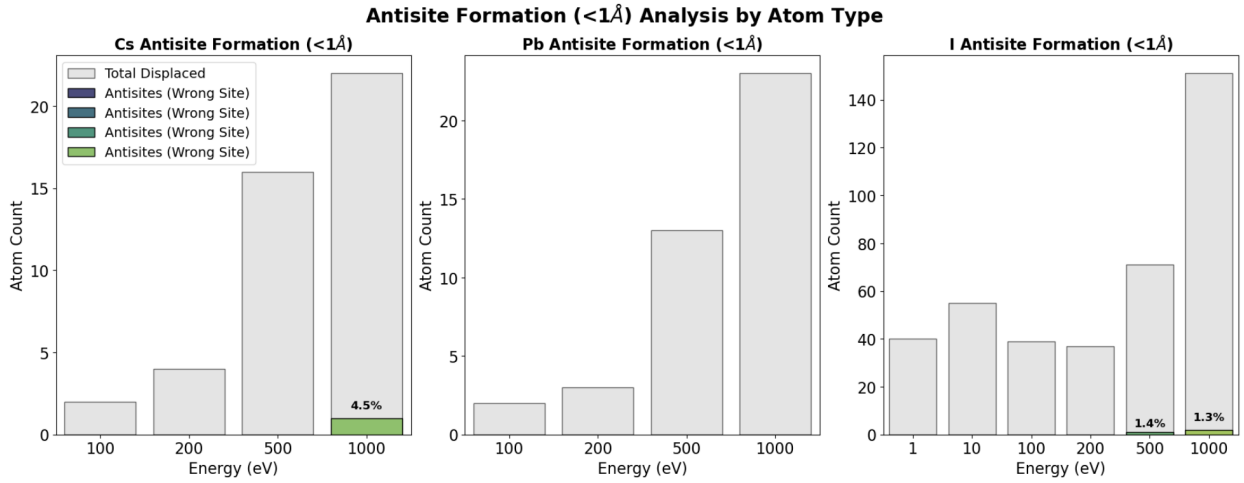

Figure 2: Anti-site defect formation probability for Cs, Pb, and I sublattices under increasing kinetic energy perturbations. The total number of displaced atoms (gray bars) and the subset identified as anti-sites (colored bars; displacement < 1 Å from a crystallographically incorrect site) are shown for incident energies ranging from 1–1000 eV. Across all atomic species and energies, anti-site formation remains negligible compared to the total number of displaced atoms. Even at the highest simulated energies (1000 eV), anti-site fractions remain below 5% for Cs and 1–2% for I, while Pb anti-sites are not observed within the <1 Å criterion. These results indicate that PKA events predominantly produce other defect configurations (*e.g.*, vacancies or interstitials), with minimal formation of stable anti-site defects.

7 Definition of Octahedral Tilt (θ) and Rotation (ϕ) Angles

The octahedral tilt angle, θ, was defined as the angle formed by the atom with the center of the octahedron. This leads to ideal values of 180° for apical iodides and 90° for equatorial linkages in the undistorted cubic perovskite lattice. Deviations from these values quantify out-of-plane octahedral tilting.

The rotational angle, ϕ, was defined as the azimuthal orientation of Pb–I bonds projected onto the xy plane. ϕ captures in-plane rotations and torsional distortions of the octahedra. Together, θ and ϕ provide a complete geometric description of radiation-induced angular disorder.

These can be visualized in Fig. 3.

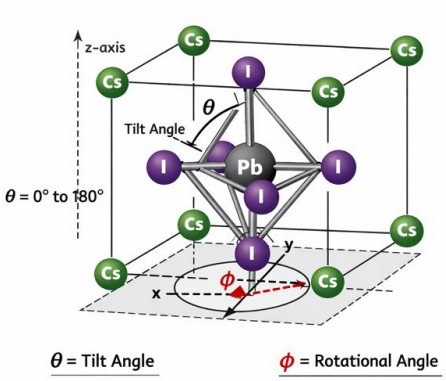

Figure 3: Schematic illustration of the PbI_6 octahedron and angular definitions in cubic $CsPbI_3$. The central Pb atom is coordinated by six I atoms forming a PbI_6 octahedron (ball-and-stick representation). The surrounding cube indicates the positions of Cs atoms at the A-sites of the perovskite lattice. The octahedral tilt angle, θ, is defined as the angle between a Pb–I bond and the crystallographic z-axis, quantifying out-of-plane distortions of the octahedron (ideal values of 0°, 90°, or 180°in the undistorted structure). The rotational angle, ϕ, is defined as the in-plane azimuthal angle of the projected Pb–I bonds in the xy plane relative to the x-axis, capturing rotational (torsional) distortions of the octahedron. This schematic provides a geometric reference for the θ and ϕ distributions analyzed in the main text and Supplemental Information.

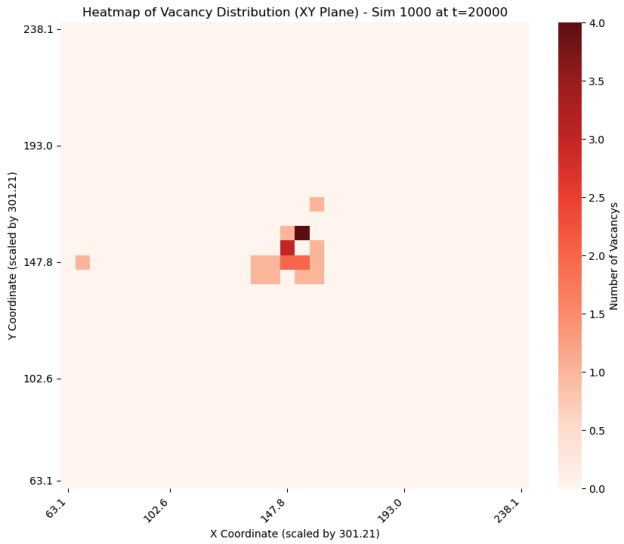

Figure 4: Spatial distribution of vacancy defects in the xy plane following an energetic particle impact. Heat map showing the spatial distribution of vacancies in the xy plane for the 1000 eV impact simulation at time, t = 20,000 fs. The color scale represents the number of vacancies per spatial bin within a 32 × 32 grid. In contrast to the interstitial distribution (Fig. S2), vacancies are strongly localized near the center of the impact region, reflecting the preferential removal of atoms from their lattice sites during the primary knock-on and subsequent collision cascade.

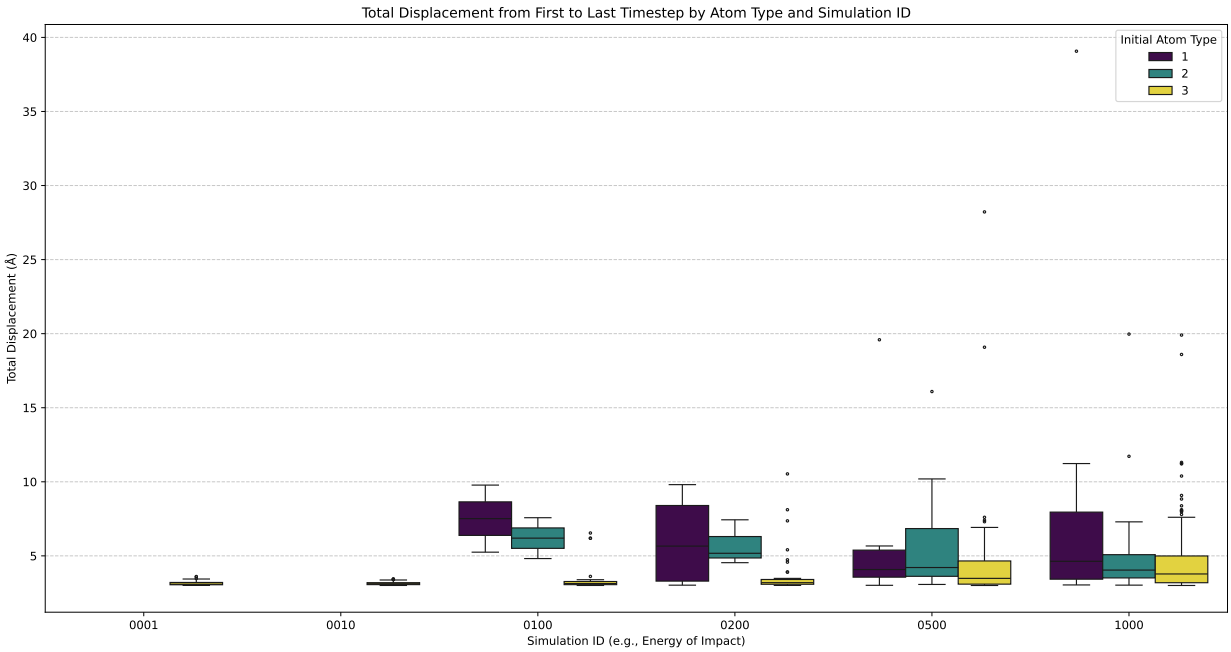

Figure 5: Total atomic displacement from the first to the final timestep for Cs, Pb, and I atoms across simulations with increasing impact energy (simulation ID). Each distribution represents the displacement statistics for a given atomic species within a single simulation. Iodide atoms show a high density of moderate displacements, while Cs and Pb atoms exhibit fewer but larger displacement events, particularly at higher impact energies. The broadening of the distributions with increasing energy reflects enhanced radiation-induced disorder and defect formation.

8 Total Atomic Displacement Statistics Across Impact Energies

To quantify the extent of atomic motion induced by radiation events, we analyze the total displacement of individual atoms from the first to the final time step of each Molecular Dynamics trajectory. Figure S5 summarizes the distribution of total displacements for different atomic species (Cs, Pb, and I) across simulations with increasing impact energy, indexed by simulation ID.

The total displacement is defined as the Euclidean distance between an atom's initial and final positions over the course of the simulation. Distributions are shown separately for each atomic species, highlighting species-dependent responses to radiation-induced collision cascades. Across all simulations, iodide ions exhibit the largest population of atoms with moderate displacements, consistent with their lower mass and weaker bonding within the perovskite lattice. In contrast, Cs and Pb atoms display fewer, but significantly larger, displacement events, particularly at higher impact energies, reflecting rare but energetic knock-on processes.

As the impact energy increases, the displacement distributions broaden for all species, with a pronounced increase in the tail of large-displacement events. This trend indicates enhanced defect formation and long-range atomic migration at higher energies. The statistical trends observed here are consistent with the summary statistics reported in Table 1, which show increasing mean displacement and variance with impact energy, especially for the A-site (Cs) cations and B-site (Pb) atoms.

This analysis provides a complementary distribution-level view of radiation damage, revealing both the dominant contribution of halide motion and the emergence of extreme displacement events at high energies that are likely associated with defect clustering and local amorphization.

Table 1: Summary statistics of total atomic displacements after filtering for atoms moving > 3 Å, grouped by simulation ID and atomic species. Reported values include the count of displaced atoms, mean displacement, standard deviation, minimum, quartiles, and maximum displacement.

Sim ID	Atom	Count	Mean	Std	Min	25%	50%	75%	Max
0001	I	40	3.151	0.153	3.005	3.050	3.088	3.205	3.605
0010	I	55	3.144	0.115	3.002	3.058	3.121	3.190	3.445
0100	Cs	2	7.513	3.202	5.249	6.381	7.513	8.645	9.777
0100	Pb	2	6.197	1.950	4.818	5.507	6.197	6.886	7.575
0100	I	39	3.400	0.863	3.002	3.057	3.131	3.269	6.543
0200	Cs	4	6.037	3.363	3.021	3.296	5.659	8.400	9.808
0200	Pb	3	5.716	1.521	4.540	4.857	5.175	6.305	7.435
0200	I	37	3.795	1.605	3.004	3.082	3.190	3.406	10.533
0500	Cs	16	5.171	3.951	3.012	3.562	4.077	5.387	19.589
0500	Pb	13	5.908	3.711	3.071	3.619	4.213	6.843	16.092
0500	I	71	4.591	3.577	3.000	3.091	3.481	4.657	28.220
1000	Cs	22	7.108	7.588	3.037	3.426	4.633	7.954	39.068
1000	Pb	23	5.258	3.733	3.024	3.511	4.040	5.081	19.971
1000	I	151	4.591	2.461	3.001	3.187	3.778	4.993	19.905